Resolution of the Cationic Distribution in Synthetic Germanite Cu22Fe8Ge4S32 by an Experimental Combinatorial Approach Based on Synchrotron Resonant Powder Diffraction Data: A Case Study and Guidelines for Analogous Compounds

L. Paradis-Fortin, P. Lemoine, E. Guilmeau, B Malaman, E. Elkaïm, A. Zitolo, S. Cordier, G. Guélou, B. Raveau, C Prestipino

▶ **To cite this version:**

L. Paradis-Fortin, P. Lemoine, E. Guilmeau, B Malaman, E. Elkaïm, et al.. Resolution of the Cationic Distribution in Synthetic Germanite Cu22Fe8Ge4S32 by an Experimental Combinatorial Approach Based on Synchrotron Resonant Powder Diffraction Data: A Case Study and Guidelines for Analogous Compounds. Chemistry of Materials, 2022, 34 (16), pp.7434-7445. ⟨10.1021/acs.chemmater.2c01561⟩. ⟨hal-03798826⟩

HAL Id: hal-03798826

https://hal.science/hal-03798826v1

Submitted on 16 Nov 2022

HAL is a multi-disciplinary open access archive for the deposit and dissemination of scientific research documents, whether they are published or not. The documents may come from teaching and research institutions in France or abroad, or from public or private research centers.

L'archive ouverte pluridisciplinaire **HAL**, est destinée au dépôt et à la diffusion de documents scientifiques de niveau recherche, publiés ou non, émanant des établissements d'enseignement et de recherche français ou étrangers, des laboratoires publics ou privés.

HAL Authorization

RESOLUTION OF THE CATIONIC DISTRIBUTION IN SYNTHETIC GERMANITE $Cu_{22}Fe_8Ge_4S_{32}$ BY AN EXPERIMENTAL COMBINATORIAL APPROACH BASED ON SYNCHROTRON RESONANT POWDER DIFFRACTION DATA: A CASE STUDY AND GUIDELINES FOR ANALOGOUS COMPOUNDS

Laura Paradis-Fortin[a,b], Pierric Lemoine[a,*], Emmanuel Guilmeau[a,], Bernard Malaman[c], Erik Elkaïm[d], Andrea Zitolo[d], Stéphane Cordier[a], Gabin Guélou[b], Bernard Raveau[b] and Carmelo Prestipino[a*]

[a] Univ Rennes, CNRS, ISCR, UMR 6226, F-35000 Rennes, France[b] Laboratoire CRISMAT, UMR 6508, CNRS, ENSICAEN, 6 Boulevard du Maréchal Juin, 14050 Caen Cedex 04, France

[c] Institut Jean Lamour, UMR 7198 CNRS, Université de Lorraine, 2 allée André Guinier Campus ARTEM, BP 50840, 54011 Nancy, Cedex, France

[d] Synchrotron SOLEIL, L'orme des Merisiers, BP 48 Saint Aubin, 91192 Gif-sur-Yvette, France

Corresponding authors: pierric.lemoine@univ-rennes1.fr; carmelo.prestipino@univ-rennes1.fr

Abstract

The present work investigates the cationic distribution of a complex CuS compound belonging to a promising class of materials with significant prospects for thermoelectric generator and photovoltaic applications. We propose the use of powder resonant X-ray scattering in a combinatorial experimental approach with X-ray and single crystal X-ray diffraction, as a valid, general, and practical method to unravel the complex cation ordering encountered in the synthetic germanite $Cu_{22}Fe_8Ge_4S_{32}$. The generation and testing of all the possible structural models is rapid and rigorous as it is based on two modules written in python language: a module that takes care of model creation and ordering (permutation algorithm associated with some filtering and ordering algorithms) and a python parser for the refinement software (FullProf) input and output. Each possible cationic model is tested through combined Rietveld refinement of resonant X-ray data at selected edges and analyzed considering its global χ^2 (Bragg contribution) agreement factor. This approach can easily integrate information coming from other techniques, as in our case EXAFS spectroscopy and single crystal X-ray diffraction.

In spite of the complexity of the germanite, we were able to define the main characteristics of the cationic ordering (space group $P\bar{4}3n$): (i) the "interstitial" site 2*a* is fully occupied by Fe, (ii) Ge is located only on the 6*d* site (or the symmetry equivalent one 6*c*), (iii) remaining Fe atoms are located preferentially on the 12*f* site and possibly on the 6*d* (or 6*c*) site along with Ge. Moreover, we single out a probable enrichment of Ge at the expense of Fe. The approach developed in this case study can be used as a guideline for the crystal structure resolution of analogous compounds.

1. INTRODUCTION

Thermoelectric (TE) generators are all-solid-state devices that enable the conversion of heat, including heat losses, into electricity thanks to the Seebeck effect. Although the TE technology has been continuously growing driven by the necessity of a more efficient energy generation, nowadays TE still remains a niche technology due to the combined environmental and economic constraints.[1,2] In contrast, ternary/quaternary Cu-rich sulfides can provide an eco-friendly low-cost alternative with relative high thermoelectric performance as prototypical bornite Cu_5FeS_4,[3–6] famatinite Cu_3SbS_4,[7,8] tetrahedrites $Cu_{12-x}T_xSb_4S_{13}$ (T = 3d metal)[9–12] and colusites $Cu_{26}T_2M_6S_{32}$ (T = Ti, V, Nb, Ta, Cr, Mo, W; M = Ge, Sn, Sb),[13–20] or more specific materials as mawsonite $Cu_6Fe_2SnS_8$,[21] stannoidite $Cu_8Fe_3Sn_2S_{12}$,[21,22] talnakhite $Cu_9Fe_8S_{16}$,[23] renierite $Cu_{20}Zn_2Fe_8Ge_4S_{32}$[24] and germanite $Cu_{22}Fe_8Ge_4S_{32}$.[25,26] Most of these materials present the characteristic to be superstructures of sphalerite-type framework "ZnS" (zinc blende)[27] and the presence of several metallic cations presenting a low contrast for X-rays, especially when oxidation state is taken into account, *e.g.* Cu^{+1}, Zn^{+2} and Ge^{+4}, all 3d^{10} cations.

Structures derived from the zinc blende framework could be represented as cationic and sulfur interpenetrating face centered cubic (fcc) sublattices, translated by a [¼, ¼, ¼] vector. The diffraction pattern of such materials presents a first set of very intense reflections, corresponding to the average zinc blend structure, and a second set of small intensity reflections originating from the supplementary modulation induced by the cationic ordering and/or the occupation of "interstitial" sites.

Although the cationic lattice arrangement effects on the global diffraction pattern are generally quite small, they play a fundamental role in the thermoelectric properties. Indeed, it was shown many times that crystal chemistry and long-range order/disorder phenomena could strongly affect the electronic and thermal properties of the materials. [17,28–37] For example, it was shown many times that cationic distribution and long-range order/disorder phenomena could strongly affect the electronic[19,22,26,35,38–40] and thermal properties[15,17,22,27,40] of sphalerite derivative Cu-based sulfide materials through modification of the chemical bonding and Cu-S conductive network[37,41]

As a consequence, the knowledge of the exact crystal structure is essential for the understanding and improvement of the thermoelectric properties of the materials. However, in some cases, the determination of the crystal structure and/or cationic distribution is made particularly difficult by: (i) the absence of single crystals in the case of samples prepared by mechanical alloying; (ii) the small contrast between cations having similar atomic numbers and/or close neutron scattering lengths; (iv) possible presence of magnetic order; (iii) similar cationic site environments; (iv) mixed occupancy of the cationic sites.

This is the case of synthetic germanite $Cu_{22}Fe_8Ge_4S_{32}$ elaborated by a combined mechanical alloying and spark plasma sintering process,[26] for which the cationic distribution ($[Cu_2]_{2a}[Cu_6]_{6c}[Fe_4T_2]_{6d}[Cu_{12}]_{12f}[Fe_4Ge_2T'_2]_{8e}$, with (i) T = Cu and T' = Ge, or (ii) T = Ge and T' = Cu) was estimated by Pavan Kumar et al.[26] on the basis of crystal chemistry consideration, ^{57}Fe Mössbauer spectroscopy data and starting from the structural model reported by Tettenhorst and Corbato ($[Cu_2]_{2a}[Cu_6]_{6c}[Cu_6]_{6d}[Cu_{12}]_{12f}[Fe_4Ge_4]_{8e}$) for mineral germanite $Cu_{26}Fe_4Ge_4S_{32}$.[42] However, both models led to poor agreement factors for the analysis of synthetic single crystal and for powder diffraction refinements inducing

doubt on the correctness of their hypothesis. This justified the reinterpretation of the ^{57}Fe Mössbauer spectra of synthetic germanite $Cu_{22}Fe_8Ge_4S_{32}$.[24]

In order to investigate such controversy, resonant X-ray scattering is the method of choice. Indeed, it is able to increase the scattering contrast of elements with similar atomic numbers and, consequently, to probe the crystal structure of complex inorganic materials on both single crystal[43–47] and powder samples.[48–57] The principle of the method is conceptually simple, the scattering contrast between the atoms is improved by the variation of "anomalous" dispersion factors *f'* and *f''* near the X-ray absorption edge of a given element without changing any structural parameter.

Thanks to such simplicity, this principle is at the base of one of the most diffused methods for *ab-initio* structure determination in biological crystallography as the multi-wavelength anomalous dispersion (MAD).[58–60] However, although quite a few experiments were performed,[47,54,61–63] its use is more limited in solid state chemistry. This is probably related to the constraints induced by the coexistence of different "heavy" atoms, the concurrence of other available methods, its relative experimental complexity (*i.e.* the absorption edges of elements that could fall outside the optimized energy range of synchrotron beamlines, the different fluorescence and absorption contribution).[64,65]

In this work, we propose the use of powder resonant X-ray scattering in a combinatorial experimental approach with X-ray and single crystal X-ray diffraction, as a valid, general, and practical method to unravel the complex cation ordering encountered in the synthetic germanite $Cu_{22}Fe_8Ge_4S_{32}$. This approach developed in this case study can be used as a guideline for the crystal structure resolution of analogous compounds.

2. EXPERIMENTAL

Synthesis. A sample of synthetic germanite $Cu_{22}Fe_8Ge_4S_{32}$ was produced by sealed tube following the conditions reported by Paradis-Fortin et al.[66] Cu (99 at.%, Alfa Aesar), Fe (99.5 at.%, Alfa Aesar), Ge (99.999 at.%, Alfa Aesar) and S (99.5 at.%, Alfa Aesar). All commercial powders were stored and manipulated in a glove box under argon atmosphere. The powders were weighed in a stoichiometric ratio (22Cu: 8Fe: 4Ge: 32S) and ground together in an agate mortar. Many 1.5 g batches of powder were then pressed into 5 mm diameter pellets. The pellets were placed in silica tubes (ϕext = 8 mm, ϕint = 6 mm) evacuated down to a pressure inferior to 10^{-2} mbar from an argon atmosphere. The sealed tubes were then placed in tubular furnaces in vertical position with a heating rate of 2 K min^{-1} and a plateau at 973 K for 24 h. The samples were cooled down at 773 K by switching off the heat power and using the thermal inertia of the furnace to limit the cooling rate, and then air quenched.

X-ray powder diffraction. High-resolution data were collected using a Bruker D8 Advance Vario 1 fitted with a two-circle diffractometer (θ-2θ Bragg-Brentano mode) equipped with a Cu $K_{\alpha 1}$ X-ray tube, a Ge [111] monochromator and a LynxEye detector.

Single crystal X-ray diffraction. The single crystal XRD data were acquired on a specimen found in a powder sample produced by solid state synthesis. The data acquisitions were performed at 300 K using a Bruker APEX-II diffractometer equipped with CCD detector using Mo Kα radiation (λ = 0.71073 Å) at the Institut Jean Lamour of Nancy. Cell refinement and data reduction were carried out with the APEX2 Software.[67]

X-ray absorption spectroscopy. X-ray absorption spectroscopy (XAS) measurements were carried out at room temperature in transmission mode at the K-edge of Ge (11103 eV), Cu (8979 eV) and Fe (7112 eV) at the beamline SAMBA (Spectroscopies Applied to Materials Based on Absorption) at Soleil Synchrotron, France (Proposal 20200538).[68] Radiation coming from a bending magnet source was monochromatized by a Si(220) fixed exit sagittally-focusing double-crystal monochromator. Harmonic rejection has been performed by the use of a couple of mirrors that also focused vertically the monochromatic beam. At the sample position, the spot area was 300 × 300 μm^2. The measurements were collected during continuous monochromator scans monitoring, incident, and transmitted X-ray flux by opportunely filled Oxford ionization chambers.[69] During measurement, a reference sample has been simultaneously measured with residual photons of the second ionization chamber for energy calibration. The amount of sample and the thickness of the pellet were optimized in order to have a proper XAS signal. The calculated amount of each sample was ground, mixed with cellulose, and then compacted into a pellet. The Extended X-ray Absorption Fine Structure (EXAFS) signal treatment was performed according to standard procedures: subtraction of the pre-edge and post-edge backgrounds, edge normalization, extraction of EXAFS signal $\chi(k)$ and its Fourier transformation, which provides a map in the real space of the distribution of the distances R around the absorber atom. Demeter software package was used to perform data treatment and fitting.[70]

Resonant scattering. The resonant scattering experiments were performed on CRISTAL beamline at SOLEIL light source facility, Saclay, France (Proposal 20181273). The diffractograms of germanite $Cu_{22}Fe_8Ge_4S_{32}$ were measured on powder samples in capillaries. All powders were sieved with 100 μm cloth sieves prior to fill the borosilicate capillaries ($\Phi_{external}$ = 0.3 mm) with opportune dilution to minimize absorption correction. The acquisitions were performed on a Debye-Sherrer geometry two-circles diffractometer positioned at the end of the beamline. The patterns were collected by a set of 21 crystal analyzer detectors Si(111) for high-resolution measurement or by nine MYTHEN 1D-strip detectors for resonant data (angular range 0 - 115° in 2θ with a step size of ~0.004°). The calibrated energy and resonant factors *f''* were calculated from an X-ray absorption spectra of the germanite sample obtained by a synchronous scan of the monochromator and the undulator gap, while incoming X-ray and fluorescence were monitored by an ionization chamber and a silicon drift detector. Then, the *f'* and *f''* factors were calculated from the X-ray absorption cross-section and by a Kramers-Kronig relation, using the code kkcalc.[71] The final scattering factor would be the scattering factor for neutral atoms adjusted by resonant correction factors.

3. RESULTS AND DISCUSSION

Synthetic germanite $Cu_{22}Fe_8Ge_4S_{32}$ is a particular case in which many of the difficulties that could be present in cationic distribution determination are coexisting: (i) the atomic form factor of the constituent cations of the material are very similar for each of the more diffuse probe in scattering experiments (neutron and X-ray) Table S1; (ii) all cations are in the same chemical environment (a tetrahedra of sulfur atoms) *i.e.* reducing the possible contribution of other complementary techniques; (iii) the material stoichiometry in relation

with the multiplicity of the crystallographic sites implies the presence of mixed site occupancy (iv) Mössbauer spectroscopy suggests the presence of magnetic ordering.[24]
Such reasons justified the application of resonant X-ray scattering in its most performing approach. While most of X-ray scattering experiments can be performed relatively far from the edges (100 eV or more) and using dispersion factors *f'* and *f''* obtained by the interpolation of the tabulated values[72], in cases such as germanite, where achieving high contrast is mandatory, such conditions are not sufficient. Indeed, it is necessary to collect data close to the absorption edges, and to use an experimental setup limiting the effects of fluorescence emission and sample absorption on the data quality. In such a case, the *f'* and *f''* tabulated values are no more valid and both values must be calculated from a XANES spectra of the studied sample.[73] Obviously, when X-absorption spectra collected presents a good quality (like the present case) it is important to fully exploit this technique that presents strong complementarity with crystal diffraction.

3.1. X-RAY ABSORBTION

XAS spectra of synthetic germanite $Cu_{22}Fe_8Ge_4S_{32}$ have been collected at Ge, Cu and Fe K-edges. Although the principal motivation was to obtain accurate dispersion factors, the spectra have been analyzed to be used as a complementary technique of characterization. In Figure 1 part a) the three represented spectra are normalized and energy shifted in respect to the edge jump. The edge positions (11109 eV for Ge, 8983 eV for Cu, 7116.5 eV for Fe) and the shape of the spectra correspond closely with the one measured on natural samples,[74] confirming the oxidation state +4 for Ge, +3 for Fe, and a majority of +1 for Cu, with all three cations in tetrahedral environments of sulfur. Unfortunately, for sphalerite derivate, the spectral shape is dominated by long range interaction[75] that tends to hide cation ordering as attested by the similar spectra observed among copper sulfide minerals.[74,76]

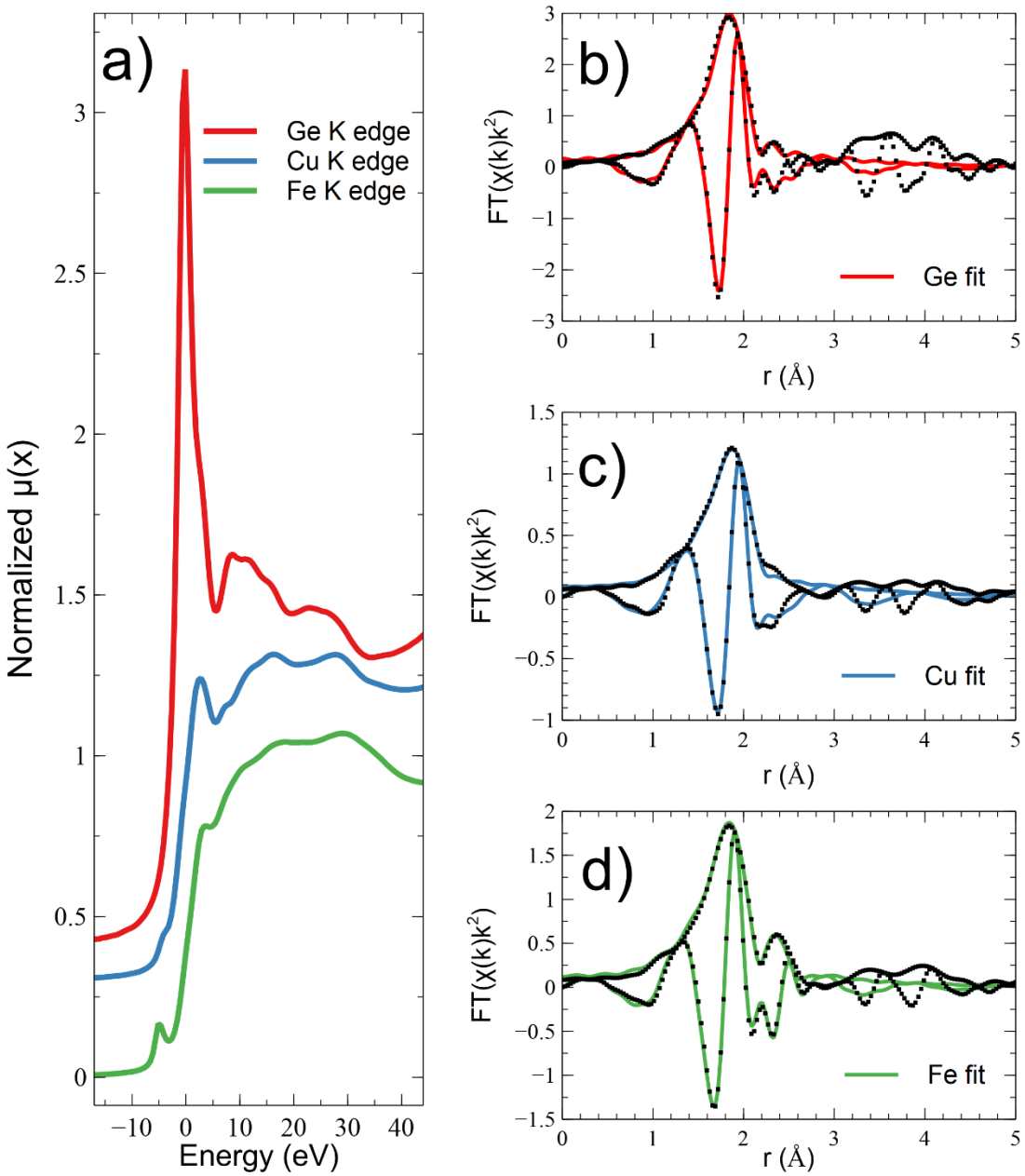

Figure 1. Part a) normalized XANES spectra of germanite at Ge, Cu and Fe K-edges. Parts b), c), d) Fourier transform of experimental EXAFS signal (black square market) and corresponding fit for Ge, Cu and Fe respectively

Fourier transform of EXAFS signal for germanite at Ge, Cu and Fe K-edges are shown in Figure 1 part b), c) and d) respectively. The spectra at Ge and Cu edges mainly consists of a strong component between 1 and 2.5 Å, corresponding to the first shell, *i.e.* four S atoms, and an envelope of more components between 3 and 5 Å corresponding to the second shell and the multiple scattering that, in the absence of a precise structure is impossible to fit. Comparing the Ge and Cu spectra, it is possible to notice a certain similitude in the spectral shape, but with a lower intensity of the latter signal. Such a variation could be ascribed to

static disorder induced by the presence of Cu in several crystallographic sites while Ge atoms keep a more homogeneous local environment. From the EXAFS analysis of the first shell (Table 1), this site heterogeneity is also emerging, with the Debye-Waller factor of Cu significantly higher than the one of Ge. The refined distances showed a difference of + 0.05 Å passing from Ge to Cu (from 2.24(2) to 2.292(6) Å) respectively, in fair agreement with typical Ge-S and Cu-S distances encountered in such compounds.[27]

Differently, for the Fe edge signal, a supplementary contribution could be noted at 2.4 Å (not phase corrected). From refinement, this contribution could be ascribed to the scattering of a metal cation at the distance of 2.72 Å. Note that in the fit, it is impossible to discriminate Fe, Cu, or Ge). Such distance is significantly large for the first shell coordination and way smaller than the typical distance between the center of two successive tetrahedra in the sphalerite network (~3.72 Å). Consequently, this can be ascribed to the occupation of the interstitial site (2*a*) by Fe atoms. This assumption is

Table 1 Summary of the parameters obtained by combined least-square refinements of χ(k) measured at the Ge, Cu, and Fe K-edges for synthetic germanite $Cu_{22}Fe_8Ge_4S_{32}$. N, S_0^2, R, σ^2 and ΔE_0 correspond to degeneracy, passive electron reduction function, distance, mean square relative displacements, and shift in the edge energy, respectively.

Edge	Path	S_0^2	N	R(Å)	δ^2	ΔE(eV)	R-factor	k-range	r-range
Ge	S	1.01(6)	4	2.24(2)	0.0034(8)	6.5(7)	0.015	3 - 14	1 - 2.5
Cu	S	0.68(4)	4	2.292(6)	0.0069(8)	3.4(6)	0.008	3 - 15	1 - 3
Fe	S	0.8(1)	4	2.27(1)	0.0050(6)	2.8(8)	0.006	3 - 13	1 - 3
	Cu	0.17(7)	6	2.72(2)	0.006(2)	2.8(8)			

supported by the equivalent metal-metal interatomic distances encountered in the tetrahedral-octahedral $[FeS_4]M_6$ complexes (M = Fe, Cu) of structurally related compounds,[27] including mawsonite,[77] talnakhite $Cu_9Fe_8S_{16}$,[78] renierite $Cu_{20}Zn_2Fe_8Ge_4S_{32}$,[79] mooihoekite $Cu_9Fe_9S_{16}$[80] and haycockite $Cu_4Fe_5S_8$.[81]

The refined amplitude reduction factor corresponding to such contribution is around ¼ of the one for the first shell, meaning that only ¼ of Fe atoms are located on interstitial position of the sphalerite network. Taking into account that the multiplicity of the interstitial site in germanite is 2 (2*a* site) and that the Fe stoichiometry is 8, this indicates that the 2*a* site is fully occupied by Fe atoms.

3.2. SYNCHROTRON POWDER DIFFRACTION

Synthetic germanite $Cu_{22}Fe_8Ge_4S_{32}$ appears as a highly crystalline solid crystallizing in the space group $P\bar{4}3n$[26] with high purity as shown by Le Bail fit of the laboratory PXRD data (Figure S1).

Space group $P\bar{4}3n$ (No 218) is a subgroup of $F\bar{4}3m$ (No 216) with transformation matrix (**2*a*, 2*b*, 2*c*; 0, 0, ½**), in which the sphalerite Wyckoff site 4*a* (referring to $F\bar{4}3m$) occupied by cations is split into the crystallographic sites 6*c*, 6*d*, 8*e* and 12*f* (referring to $P\bar{4}3n$, see Figure S2). These four crystallographic sites, forming the sphalerite network of germanite, are completed by the "interstitial" 2*a* site (referring to $P\bar{4}3n$) to fully describe the germanite structure. Consequently, the reflections of germanite could be divided into base

reflections and superstructure reflections, the former describing the average sphalerite structure and the latter describing its occupational and/or displacive modulation.
The gain in resolution given by synchrotron powder diffraction with a crystal analyzer setup (Figure 2), showed that the synthetic germanite sample prepared by sealed tube synthesis[66] should be interpreted as a composite material composed of several phases. Two or three or even more, low crystallinity phases ascribed to disordered sphalerite type phases ($F\bar{4}3m$, a ~5.3 Å) and one majoritarian (from the intensity ratio of peaks > 80 %) extremely crystalline ($P\bar{4}3n$, a = 10.595 Å). Due to the symmetry relationship between the two space groups, and the similar sphalerite structure periodicity, the base reflections of the crystalline phase are heavily superimposed with the peaks of the low-crystalline phases.

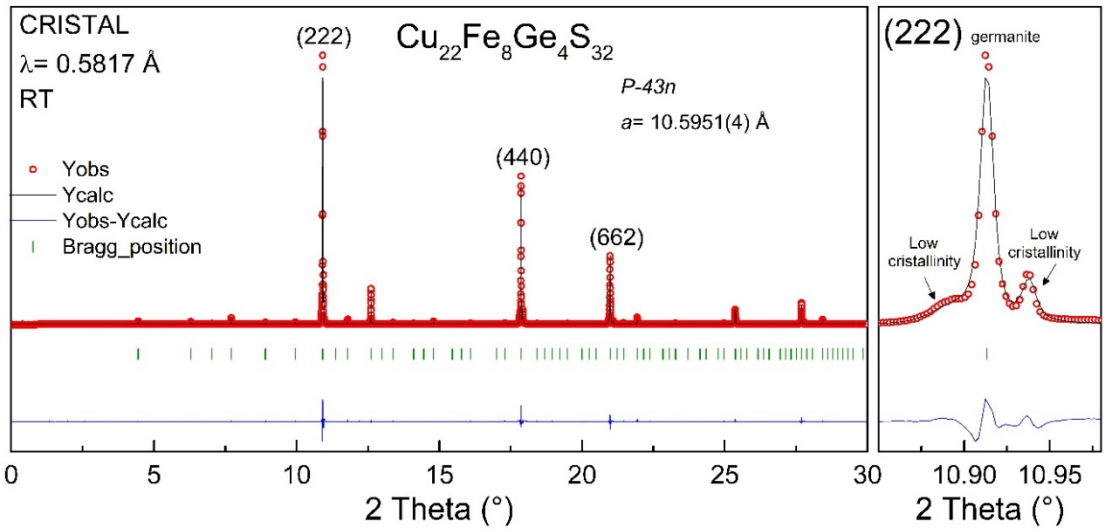

Figure 2. Part a) Synchrotron powder diffraction of germanite. Part b) zoom on the (222) peaks

This fact precludes to study the cation ordering of the high crystalline phase by conventional combined Rietveld refinement of X-ray resonant diffraction data and Fourier difference method.The intensity evaluation of basic reflections is not reliable enough for the optimization of sites occupancy, although the intensities of superstructure reflections, describing the cation ordering, are available. For such reasons, we developed an alternative approach inspired by combinatorial chemistry that consists of the direct test of all physical and chemically sensible models over experimental data. Such approach allow combining the information coming from patterns collected at different energies, thus avoiding refining site occupation.

3.3. COMBINATORIAL APPROACH

The method is based on two modules written in python language: (i) the ***models*** module that takes care of model creation and ordering; (ii) the python **parser** for the **FullProf**[82] input and output, able to interface with ***models*** object.
The ***models*** module is based on the standard itertools python library, which implements efficiently permutation algorithm to which was associated some filtering and ordering

algorithms. Its functioning can easily be illustrated for Fe atoms in germanite case. Without any *a priori* information, the number of possible arrangements of 8 Fe atoms over the five cationic Wyckoff sites of germanite (2*a*, 6*c*, 6*d*, 8*e* and 12*f*) corresponds to the binomial coefficient $\binom{12}{8}$ *e.g.* 495 unique combination: *(aaccdddd), (aaccddde), (aaccdddf), (aaccddee), (aaccddef), (aaccddff) ……*, however 136 sequences must be excluded as they do not respect the sites multiplicity, *e.g.* more than 2 atoms in *a* site, and consequently only 359 configurations are physically possible. The **FullProf python parser** is a module that iterates along a sequence of configuration and performs a structural refinement (Rietveld or single crystal), collects the results, and connects them to each configuration. At the end of the run, only the models respecting a set of requirements, *e.g.* good accordance with all the data and/or the absence of not-physical parameter values, are retained. The use of such an approach has been documented in a set of Jupyter notebooks available as Electronic Supporting Information.

In the present case, synthetic germanite with stoichiometry $Cu_{22}Fe_8Ge_4S_{32}$ generates 17928 possible cationic arrangements. Such numbers result from the multiplication of the 359 possible models of Fe with the 65 possible models for Ge and filtered again to respect the Wyckoff sites multiplicity. The batch refinements of one dataset for such a number of configurations are manageable by a modern powerful computer in a time-lapse spanning from a couple of hours to half a day depending on the dataset and the refined parameters. However, in the present work, we choose to present a more iterative approach allowing to speed up significantly the process (a few minutes for calculation) and underlining the strength of resonant diffraction. For germanite, four datasets were available: (i) a low quality laboratory single-crystal dataset, (ii) a synchrotron powder diffraction dataset collected around the Cu edge, (iii) a synchrotron powder diffraction dataset collected around the Ge edge and (iv) a synchrotron powder diffraction dataset collected at 21 keV, using a high-resolution setup.

Single crystal dataset A unique single crystal of germanite of very small size (< 0.02 × 0.02 × 0.02 mm^3) has been found in one of sealed tube synthesis batch. The data obtained, although acquired with high integration time, were of low quality (1148 reflections above 2σ) and consequently were not good enough to fully solve the cationic ordering. However, since Ge^{4+} and Cu^{+} are isoelectronic, and only 4 Ge^{4+} and 2 Cu^{2+} cations occupy the unit cell, it is reasonable to approximate that the contrast mainly originates from the Fe^{3+} cations. Hence Cu^{+} and Ge^{4+} were considered to be the same scatterer (Cu), reducing the number of configurations to only 360 to investigate Fe ordering.

Figure 3 shows the RF^2 agreement factor from single-crystal diffraction refinement (details of the refinement are included in Supporting Information) as a function of the model number. As shown in Figure 3a, there is a significant reduction of the RF^2 agreement factor when the site 2*a* site is fully occupied by Fe (the lower the agreement factor is, the better the model fits the data), in agreement with the results from EXAFS analysis at Fe K-edge. This supports the approximation made for single crystal analysis and also confirms that the Tettenhorst model for natural germanite,[42] in which the site 2*a* is occupied by Cu, is not representative of synthetic germanite. Consequently, this result confirms that the two cationic distributions initially proposed for synthetic germanite $Cu_{22}Fe_8Ge_4S_{32}$ are wrong.[26]

Figure 3b shows that the quality of the fit is dependent on the Fe content of the site 12*f*; higher Fe content leads to better fits. Consequently, we hypothesize that at least two Fe atoms occupy the site 12*f*. Even though the RF^2 is clearly improved at higher Fe content, we set the constraint low considering the possible error induced by ignoring the scattering difference between Cu and Ge. Taking into account these new insights, the number of possible configurations for cation ordering in germanite passes from 17928 to 1211.

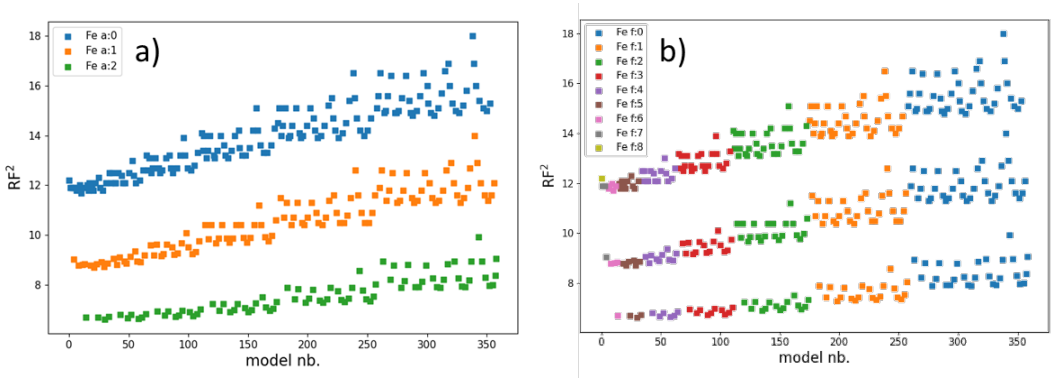

Figure 3. RF^2 agreement factors from single-crystal diffraction refinement as a function of the configuration number. Part a) and part b) models colored as a function of the number of Fe on site 2*a* and 12*f,* respectively.

Ge and Cu resonant diffraction: The number of possible configurations could be further reduced just by a preliminary inspection of patterns collected near the Ge K-edge (Figure 4). As visible, the reflection (210), almost extinct in the pattern collected at 1.1209 Å (*i.e.* in the non-resonant diffraction conditions), increases its intensity proportionally with the decrease of the *f'* factor (*i.e.* in the resonant diffraction conditions).
Considering the structure factor of the reflection (210),

$$F(210) \approx \sum_j^6 f_{c_j} e^{-2i\pi\,((2,1,0)\cdot r_{c_j})} + \sum_j^6 f_{d_j} e^{-2i\pi\,((2,1,0)\cdot r_{d_j})} = \widehat{f_c} - \widehat{f_d},,$$

where f_{c_j} (f_{d_j}) is the atomic form factor for the j^{th} atom located on the 6*c* (6*d*) site and $\widehat{f_c}$ ($\widehat{f_d}$) is the average atomic form factor for all atoms located on the 6*c* (6*d*) site. In non-resonant diffraction conditions, reflection (210) is always very small due to the similarity of Ge^{4+} Cu^{+} and Fe^{3+} atomic form factors and the negligible ADP difference. However, approaching the Ge K-edge its intensity significantly (Figure 4) increase. In such energy range, the atomic form factors of Ge^{4+} decrease and acquire a positive small imaginary part while the other atomic form factors remain constant. As a consequence, the increase of the (210) intensity approaching the Ge K-edge could be only explained by a difference in Ge occupation on 6*c* and 6*d* sites. Considering the magnitude of anomalous correction factors, the 6*c* and 6*d* sites should differ by at least 2 Ge atoms. Such condition further reduces the number of possible configurations from 1211 to 476.

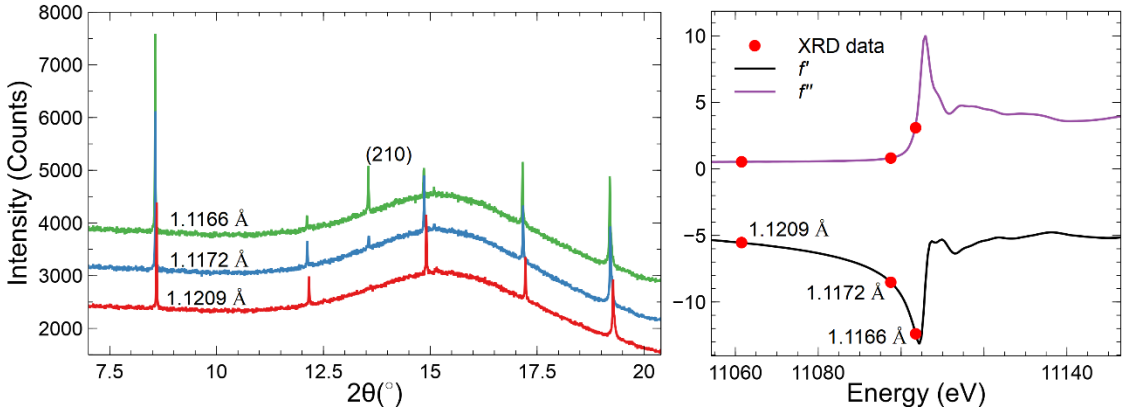

Figure 4. Part a) zoom on the superstructure peaks of XRD patterns of germanite collected near the Ge K-edge at 1.1166 Å, 1.1172 Å, 1.1209 Å respectively at 2, 7 and 42 eV from the Ge K-edge. Part b) evolution of dispersion factors for the patterns shown in part a)

To take into account simultaneously all the resonant effects, a set of data has been created. This set is composed by (i) the equally weighted superstructure region of the synchrotron powder X-ray diffraction patterns collected at 1.3820 Å and 1.3807 Å (near Cu K-edge), 1.1172 Å and 1.1166 Å (near Ge K-edge), 0.5817 Å (far from any edges) and (ii) the single crystal X-ray diffraction data. The first four synchrotron PXRD patterns allow to take into account resonant effects at Cu and Ge K-edges while the fifth has been collected in a region far from resonant effects. The four resonant wavelengths have been chosen just before and at the bottom of the absorption edges in order to obtain significantly different values for *f'* but a small *f''* factor, *i.e.* minimize the absorption and fluorescence. Due to the low quality of the single crystal and the limitation of the apparatus used, the signal-to-noise ratio for the integrated intensities of single-crystal diffraction is generally lower than the intensity extracted from synchrotron powder diffraction. As a consequence, the use of single-crystal data presents a limited effect on the statistic of the refinement, but significantly reduce the correlation of fitting parameters.

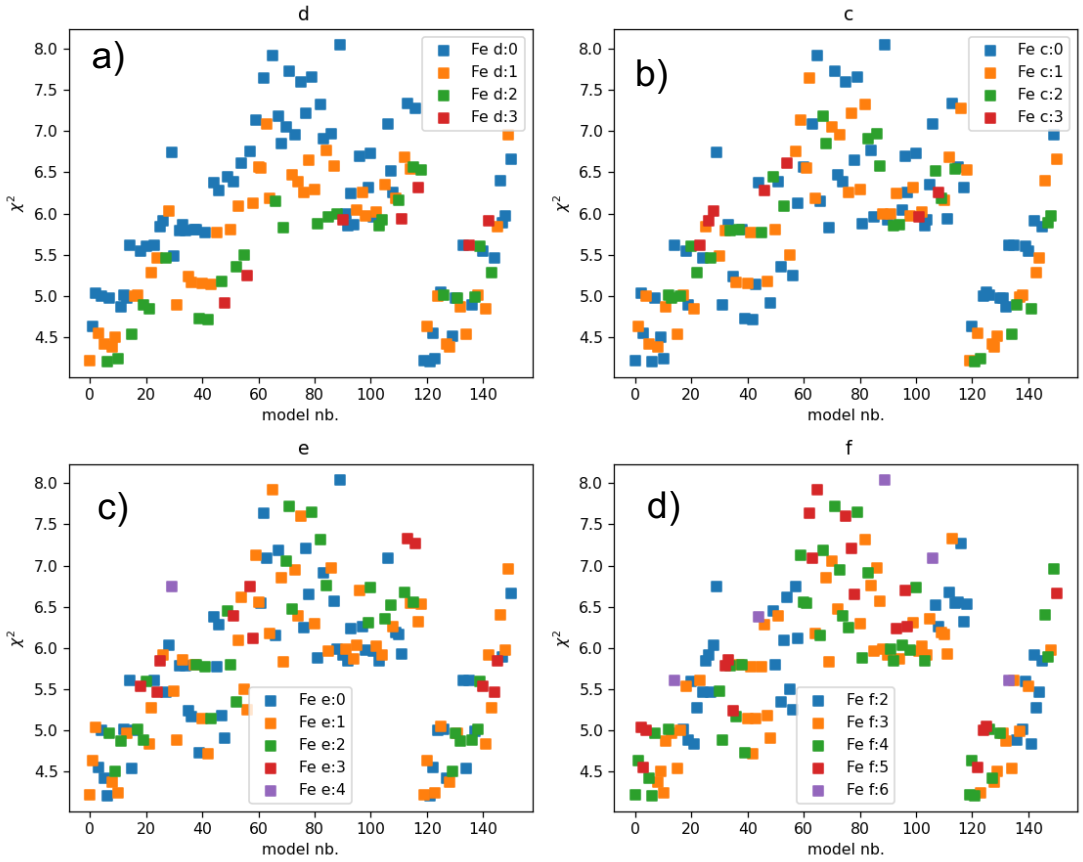

Figure 5. Global χ^2 (Bragg contribution) agreement factor from the composite set of diffraction data refinement as a function of the configuration number. Part a), b), c) and d) models colored as a function of the number of Ge on site 6*d*, 6*c,* 8*e* and 12*f* respectively

Rapid screening of the 476 models (~ 2 min) could be performed by using the structural model (positions and ADP) from the best preliminary single crystal refinement, thus allowing to refine only the scales factors (more details in SI). The correlated evolution of the combined χ^2 as a function of the model number is shown in Figure S3 and Figure S4. The following characteristics seem to favor a low global χ^2 agreement factor: (i) a high concentration of Ge on either 6*c* site or 6*d* site (Figure S3) and (ii) the localization of Fe mainly on the 12*f* site (Figure S4). However, it is also worth of noting that the possible correlation between the cationic site occupations and cartesian coordinates of sulfur atoms and sites *e* and *f*, could partially change the agreement factors. This explains the slightly better χ^2 values observed for high concentration of Ge on the 6*d* site compared to 6*c* site. For this reason, we used such a screening only to further restrict the group of possible configurations, *i.e.* to yield the "best" 150 configurations, with global user weighted χ^2 (Bragg contribution) < 10.

The group of these selected 150 configurations has been successively tested refining also cartesian positions, and ADP (~ 4 min), and the evolution of the combined χ^2 as a function of the model number is shown in Figure 5 and Figure S5. As expected, the agreement factors were globally improved by the correlation effect among fitting parameters, the

relative difference of agreement between models has been varied, as in particular for models with 4 Ge atoms on site 6*c*. However, the general order of models is maintained confirming the choice to limit the refinement to only the "best" 150 models (Figure S6). The 10 models leading to the lowest global χ^2 agreement factors are listed in Table 2.

Table 2. Best models of cationic distribution with nominal stochiometry for synthetic germanite $Cu_{22}Fe_8Ge_4S_{32}$.

Models					**χ^2 Bragg**
2*a*	6*d*	6*c*	12*f*	8*e*	
Fe_2	Cu_6	Ge_4Fe_2	Fe_4Cu_8	Cu_8	4.21
Fe_2	Fe_2Ge_4	Cu_6	Fe_4Cu_8	Cu_8	4.21
Fe_2	$Fe_1Ge_4Cu_1$	Cu_6	Fe_4Cu_8	Fe_1Cu_7	4.22
Fe_2	Cu_6	$Ge_4Fe_1Cu_1$	Fe_4Cu_8	Fe_1Cu_7	4.22
Fe_2	Fe_2Ge_4	Cu_6	Fe_3Cu_9	Fe_1Cu_7	4.24
Fe_2	Cu_6	Ge_4Fe_2	Fe_3Cu_9	Fe_1Cu_7	4.25
Fe_2	$Fe_1Ge_4Cu_1$	Fe_1Cu_5	Fe_3Cu_9	Fe_1Cu_7	4.38
Fe_2	Fe_1Cu_5	$Ge_4Fe_1Cu_1$	Fe_3Cu_9	Fe_1Cu_7	4.38
Fe_2	Fe_1Cu_5	$Ge_4Fe_1Cu_1$	Fe_4Cu_8	Cu_8	4.42
Fe_2	$Fe_1Ge_4Cu_1$	Fe_1Cu_5	Fe_4Cu_8	Cu_8	4.43

These ten cationic distributions do not present any unphysical value for ADP and atoms positions and the order presents some common characteristics. First, the 6 remainging Fe atoms (2 Fe atoms being on the 2*a* site) are mainly on the 12*f* site. Second, all Ge atoms are located either on the 6*d* site or 6*c* site. The equivalence between 6*d* site and 6*c* site is explained by symmetry consideration; the point group symmetry for both sites is $\bar{4}$ and it is possible to obtain an equivalent atomic configuration just by swapping the two sites. However, also if such cation distributions appear reasonable, it is not able to reproduce the increase in intensity of the reflection (210) approaching the Ge K-edge, the calculated intensity remaining lower than the experimental values (Figure 6). Knowing that $F(210) \approx \widehat{f_c} - \widehat{f_d}$ and that the best models already comprise the maximum difference in Ge atoms between the 6*c* and 6*d* sites, the mismatch in the evolution of the (210) intensity suggests that the highly crystalline component of synthetic germanite presents a deviation from the nominal composition $Cu_{22}Fe_8Ge_4S_{32}$ to a Ge-rich composition. Note that a deviation from the nominal stoichiometry of synthetic germanite was already suggested in priror ^{57}Fe Mössbauer spectroscopy analyses[24]. To investigate such hypotheses, we repeated the refinement also for stoichiometries $Cu_{22}Fe_7Ge_5S_{32}$ and $Cu_{22}Fe_6Ge_6S_{32}$. Note that Fe for Ge substitution (up to 2 atoms) leads to stoichiometries respecting the charge balance, while the Ge for Cu substitution does not. Taking into account the full occupation of the site 2*a* by Fe atoms and the symmetry equivalence of the 6*d* and 6*c* sites, imposing that all Ge atoms are either in 6*d* or 6*c* sites, results into 36 and 15 cationic configurations for $Cu_{22}Fe_7Ge_5S_{32}$ and $Cu_{22}Fe_6Ge_6S_{32}$, respectively.

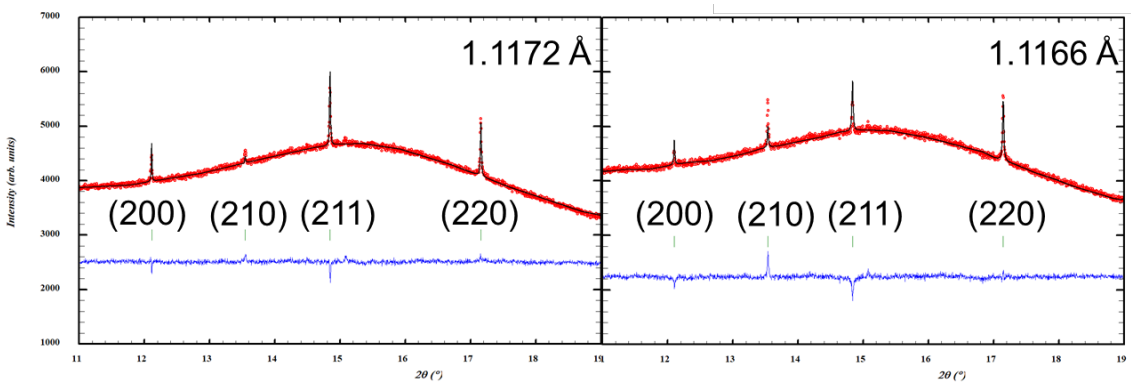

Figure 6. Rietvel refinement for model $[Fe_2]_a[Cu_6]_c[Ge_4Fe_2]_d[Fe_4Cu_8]_f[Cu_8]_e$, data collected at 20 eV and 5 eV before the Ge K-edge

The result of the refinements is shown in Figure 7. The enrichment in Ge of the 6*d* site (or 6*c*) generates an average lowering of the agreement factor. Moreover, the hypothesis of a germanium enrichment of the synthetic germanite is also supported by the chemical composition of numerus natural germanite samples[83] and the existence of other structurally related mineral phases with a global germanium content of 6 over 34 metallic atoms per formula unit, including maikainite $Cu_{20}Mo_2(Fe,Cu)_6Ge_6S_{32}$,[84] ovamboite $Cu_{20}W_2(Fe,Cu,Zn)_6Ge_6S_{32}$,[84] and colusite $Cu_{26}T_2Ge_6S_{32}$ (T = V, Nb, Ta, Cr, Mo, W)[13,14,16,19,38,85,86]. The best 10 models for these two enriched Ge stoichiometries are listed in **Table 3**. The agreement factors are not reliable enough to definitively discriminate between the two compositions and the possibility of intermediate composition cannot be excluded, although the 2*a* ADP values for stoichiometry $Cu_{22}Fe_6Ge_6S_{32}$ present suspicious Biso values (lower than 0.31 Å^2), and consequently, supports the stoichiometry $Cu_{22}Fe_7Ge_5S_{32}$. From a site occupation point of view, the general trend established in previous refinements is maintained with the preferential occupation of the 12*f* site by Fe

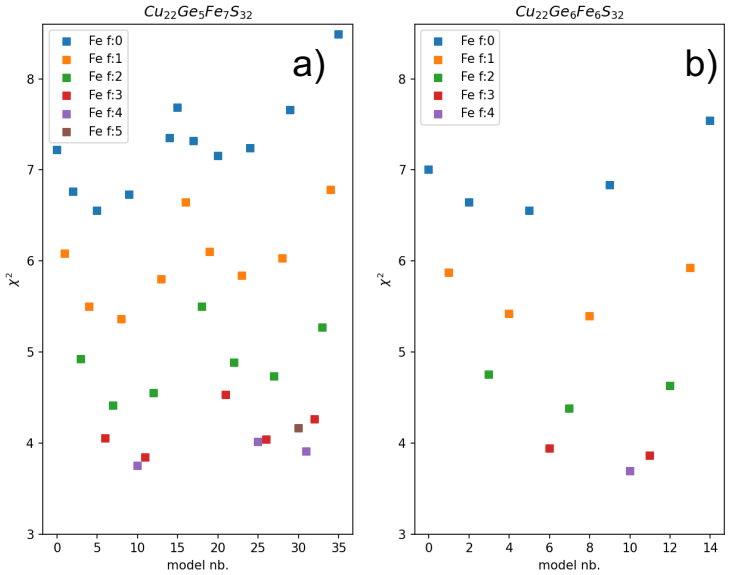

Figure 7. Global χ^2 (Bragg contribution) agreement factor from the composite set of diffraction data refinement as a function of the configuration number. Part a) Nominal composition $Cu_{22}Fe_7Ge_5S_{32}$ b) Nominal composition $Cu_{22}Fe_6Ge_6S_{32}$

atoms and a slight preference for Fe, in respect to Cu, for sharing the 6*d*/6*c* site with Ge. In the light of such considerations, and taking into account (i) the observation of EXAFS spectra that suggests a lower disorder configuration for Ge atoms in respect to Cu, and (ii) the similar interatomic distances with sulfur of Fe^{3+} and Ge^{4+} cations in tetrahedral coordination,[27] the more reliable models for the crystalline component of synthetic germanite are $[Fe_2]_a[Cu_6]_c[Ge_{4+x}Fe_{2-x}]_d[Fe_4Cu_8]_f[Cu_8]_e$ or the equivalents $[Fe_2]_a[Ge_{4+x}Fe_{2-x}]_c[Cu_6]_d[Fe_4Cu_8]_f[Cu_8]_e$ (symmetry conjugate), with x = 0, 1 or 2.
It is particularly interesting to note that the partial substitution of Fe by Ge suspected in synthetic germanite is counterbalanced by a decrease in the Cu^{2+}/Cu^{+} ratio. This observation is of particular interest comparing present XANES data at Cu K-edge with the one collected on natural germanite.[74] Indeed the small shoulder present at 8979 eV is ascribed to the pre-edge peak $1s \rightarrow 3d$ and it is only active for Cu^{2+} atoms, and consequently its intensity is proportional to the concentration of Cu^{2+}. In the case of natural germanite studied by Belissont et al.[74] the intensity of the shoulder is significantly lower than in the present synthetic germanite.

Table 3 Best models of cationic distribution with Ge enriched stochiometries $Cu_{22}Fe_7Ge_5S_{32}$ and $Cu_{22}Fe_6Ge_6S_{32}$ (light grey overshadow)

Models					χ^2 Bragg
2a	***6d***	***6c***	***12f***	***8e***	
Fe_2	Ge_6	Cu_6	Fe_4Cu_8	Cu_8	3.69
Fe_2	Ge_5Fe_1	Cu_6	Fe_4Cu_8	Cu_8	3.75
Fe_2	Ge_5Fe_1	Cu_6	Fe_3Cu_9	Fe_1Cu_7	3.84
Fe_2	Ge_6	Cu_6	Fe_3Cu_9	Fe_1Cu_7	3.86
Fe_2	Ge_5Cu_1	Cu_6	Fe_4Cu_8	Fe_1Cu_7	3.91
Fe_2	Ge_6	Fe_1Cu_5	Fe_3Cu_9	Cu_8	3.94
Fe_2	Ge_5Cu_1	Fe_1Cu_5	Fe_4Cu_8	Cu_8	4.01
Fe_2	Ge_5Cu_1	Fe_1Cu_5	Fe_3Cu_9	Fe_1Cu_7	4.04
Fe_2	Ge_5Fe_1	Fe_1Cu_5	Fe_3Cu_9	Cu_8	4.05
Fe_2	Ge_5Cu_1	Cu_6	Fe_5Cu_7	Cu_8	4.16

Effectively, as mentioned in the previous work,[26] the control of Cu^{2+} concentration is a fundamental parameter to obtain "pure" and crystalline materials, and the synthesis of germanite poorer in Fe, such as $Cu_{26}Ge_4Fe_4S_{32}$, were impossible.

The proposed cation distribution has also an another interesting consequence, indeed it demonstrates that germanite $Cu_{22}Fe_8Ge_4S_{32}$($P\bar{4}3n$) is a disordered structure of renierite $Cu_{20}Zn_2Ge_4S_{32}$ ($P\bar{4}2c$), if Zn atoms are replaced by Cu (see Figure 8a). Space group $P\bar{4}2c$ is a translationengleiche subgroups of index 3 of the space group $P\bar{4}3n$ with transformation matrix (a'= a, b'=b, c'=c, origin shift=(0, ½, ¼)). *Mutatis mutandis* the structure of Bernstein et al.[79] the splitting of the Wyckoff positions and the occupations of both structure is shown in Figure 8b. Neglecting strain deformation, the preferential site occupation for Fe, Ge and Zn on 4*i, 4g* and 2*e* sites ($P\bar{4}2c$) are responsible of the lowering in symmetry and in particular of the loss of the axis 3^{+}_{111}. Pavan Kumar et al.[24] shown that the balance between the two structures is mainly related to the Zn stoichiometry; however,

a possible enrichment in Ge will tend to reduce the cation ordering between site 4*g* and 2*f*. Moreover in the approximation that the structural relationship is maintained between the two groups, the Cu^{2+} atoms replacing Zn^{2+} should be hosted on site 6*c* in germanite.

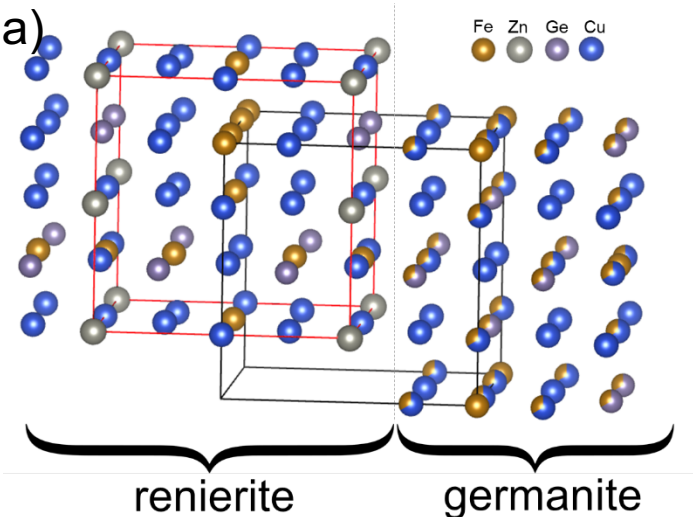

b)

germanite		*renierite*	
$P\bar{4}3n$		$P\bar{4}2c$	
12*f*	Cu_8Fe_4	**4*j***	Cu_4
		4*m*	Cu_4
		4*i*	Fe_4
8*e*	Cu_8	**8*n***	Cu_8
6*d*	Ge_4Fe_2	**4*g***	Ge_4
		2*f*	Fe_2
6*c*	Cu_6	**4*h***	Cu_4
		2*e*	Zn_2
2*a*	Fe_2	**2*d***	Fe_2

Figure 8. Part a): Structural relationship between Renierite (red lines cell) and Gemanite (black lines cell) with cation ordering $[Fe_2]_a[Cu_6]_c[Ge_4Fe_2]_d[Fe_4Cu_8]_f[Cu_8]_e$. Zn atoms are replaced by Cu. Sulfur atom are not present for sake of simplicity. Part b) splitting of Wyckoff sites from germanite to renierite.

4. CONCLUSION

Using the complementarity between X-ray absorption spectroscopy and resonant powder X-ray diffraction, we have resolved the cationic distribution of synthetic germanite thank to the development of an approach based on a systematic testing of all possible cationic ordering models. Each possible cationic ordering model is tested through combined Rietveld refinement of resonant X-ray data at selected edges and analyzed considering its global χ^2 (Bragg contribution) agreement factor. This approach can easily integrate information coming from other techniques, as in our case EXAFS spectroscopy and single crystal X-ray diffraction, allowing to highlight structural features which can be considered to reduce the number of structural models to be tested. In spite of the complexity of the title material (equivalent atomic form factor and chemical environment of the cations, multiple cationic sites, and mixed site occupancy), we were able to define the main characteristics of the cationic ordering of synthetic germanite (space group $P\bar{4}3n$): (i) the "interstitial" site 2*a* is fully occupied by Fe, (ii) Ge is located only on the 6*d* site (or the symmetry equivalent one 6*c*), (iii) remaining Fe atoms are located preferentially on the 12*f* site and possibly on the 6*d* (or 6*c*) site along with Ge. Moreover, we single out a probable enrichment of Ge at the expense of Fe in synthetic germanite. This deviation to the nominal composition is related to the detection, by high-resolution synchrotron powder X-ray diffraction data, of a low crystalline phase of sphalerite structure ($F\bar{4}3m$). Consequently, the most reliable cationic distribution, $[Fe_2]_a[Cu_6]_c[Ge_{4+x}Fe_{2-x}]_d[Cu_8]_e[Fe_4Cu_8]_f$ (with x = 0, 1 or 2), that we propose for synthetic germanite $Cu_{22}Fe_{8-x}Ge_{4+x}S_{32}$, strongly deviates from

the structural model proposed by Tettenhorst and Corbato[42] *i.e.* $[Cu_2]_a[Cu_6]_c[Cu_6]_d[Ge_4Fe_4]_e[Cu_{12}]_f$ for natural germanite $Cu_{26}Fe_4Ge_4S_{32}$.
This new structural description of germanite will be of prime interest to explain the different electronic transport properties encountered in the structurally related germanite and colusite systems, and will be the starting point of further correction of probably erroneous cationic distribution reported in related mineral phases involving highly unlikely d^{10} interstitial *T* atoms, *i.e.* Cu^+, in their tetrahedral-octahedral $[TS_4]M_6$ (*M* = Cu, Fe) complexes.
On a technical point of view, the approach presents a clear interest for the study of cation ordering in material chemistry. Actually, in less complex materials such an approach allows a comprehensive investigation of cation ordering with the minimal background in crystallography. Moreover, it is worth noticing that the association of powder diffraction capability on X-ray absorption beamline is more and more common and consequently the acquisition of resonant diffraction data will become more widespread and conventional. Python libraries and few examples of Jupyter notebook will be available as supporting information, with the scope of reproduction of the analysis and help for the reader interested in the application of such an approach.

■ ASSOCIATED CONTENT

The Supporting Information is available free of charge on the ACS Publications website at DOI: XXXXXX

- Supplementary figure and table
- Python code
- Jupyter notebook
- CIF for the best nominal composition model

■ AUTHOR INFORMATION

Corresponding Authors
*carmelo.prestipino@univ-rennes1.fr
*pierric.lemoine@univ-rennes1.fr

■ ACKNOWLEDGMENTS

The authors gratefully thank SAMBA beamline support team and in particular Gautier Landrot. The authors acknowledge the SOLEIL synchrotron (Saclay, France) for the provision of research facilities, and the financial support of the French Agence Nationale de la Recherche (MASSCOTE, 2016, ANR- 15-CE05-0027).

REFERENCES

(1) Snyder, G. J.; Toberer, E. S. Complex Thermoelectric Materials. *Nat. Mater.* **2008**, *7*, 105–114.
(2) Pei, Y.; Shi, X.; LaLonde, A.; Wang, H.; Chen, L. L.-D.; Snyder, G. J. Convergence of Electronic Bands for High Performance Bulk Thermoelectrics. *Nature* **2011**, *473* (7345), 66–69. https://doi.org/10.1038/nature09996.
(3) Qiu, P.; Zhang, T.; Qiu, Y.; Shi, X.; Chen, L. Sulfide Bornite Thermoelectric Material: A Natural Mineral with Ultralow Thermal Conductivity. *Energy Environ. Sci.* **2014**, *7* (12), 4000–4006. https://doi.org/10.1039/c4ee02428a.
(4) Pavan Kumar, V.; Barbier, T.; Lemoine, P.; Raveau, B.; Nassif, V.; Guilmeau, E. Crucial Role of Selenium for Sulphur Substitution in the Structural Transitions and Thermoelectric Properties of Cu_5FeS_4 Bornite. *Dalton Trans.* **2017**, *46* (7), 2174–2183. https://doi.org/10.1039/C6DT04204J.
(5) Long, S. O. J.; Powell, A. V.; Vaqueiro, P.; Hull, S. High Thermoelectric Performance of Bornite through Control of the Cu(II) Content and Vacancy Concentration. *Chem. Mater.* **2018**, *30* (2), 456–464. https://doi.org/10.1021/acs.chemmater.7b04436.
(6) Guélou, G.; Powell, A. V.; Vaqueiro, P. Ball Milling as an Effective Route for the Preparation of Doped Bornite: Synthesis, Stability and Thermoelectric Properties. *J. Mater. Chem. C* **2015**, *3* (40), 10624–10629. https://doi.org/10.1039/c5tc01704a.
(7) Tanishita, T.; Suekuni, K.; Nishiate, H.; Lee, C.-H.; Ohtaki, M. A Strategy for Boosting Thermoelectric Performance of Famatinite Cu_3SbS_4. *Phys. Chem. Chem. Phys.* **2020**, *22* (4), 2081–2086. https://doi.org/10.1039/C9CP06233E.
(8) Goto, Y.; Sakai, Y.; Kamihara, Y.; Matoba, M. Effect of Sn-Substitution on Thermoelectric Properties of Copper-Based Sulfide, Famatinite Cu_3SbS_4. *J. Phys. Soc. Jpn.* **2015**, *84* (4), 044706. https://doi.org/10.7566/JPSJ.84.044706.
(9) Lai, W.; Wang, Y.; Morelli, D. T.; Lu, X. From Bonding Asymmetry to Anharmonic Rattling in $Cu_{12}Sb_4S_{13}$ Tetrahedrites: When Lone-Pair Electrons Are Not So Lonely. *Adv. Funct. Mater.* **2015**, *25* (24), 3648–3657. https://doi.org/10.1002/adfm.201500766.
(10) Guélou, G.; Powell, A. V.; Smith, R. I.; Vaqueiro, P. The Impact of Manganese Substitution on the Structure and Properties of Tetrahedrite. *J. Appl. Phys.* **2019**, *126* (4), 045107.
(11) Suekuni, K.; Tsuruta, K.; Kunii, M.; Nishiate, H.; Nishibori, E.; Maki, S.; Ohta, M.; Yamamoto, A.; Koyano, M. High-Performance Thermoelectric Mineral $Cu_{12-x}Ni_xSb_4S_{13}$ Tetrahedrite. *J. Appl. Phys.* **2013**, *113* (4), 043712. https://doi.org/10.1063/1.4789389.
(12) Lu, X.; Morelli, D. T.; Xia, Y.; Ozolins, V. Increasing the Thermoelectric Figure of Merit of Tetrahedrites by Co-Doping with Nickel and Zinc. *Chem. Mater.* **2015**, *27* (2), 408–413. https://doi.org/10.1021/cm502570b.
(13) Guélou, G.; Lemoine, P.; Raveau, B.; Guilmeau, E. Recent Developments in High-Performance Thermoelectric Sulphides: An Overview of the Promising Synthetic Colusites. *J. Mater. Chem. C* **2021**, *9* (3), 773–795. https://doi.org/10.1039/D0TC05086E.
(14) Bouyrie, Y.; Ohta, M.; Suekuni, K.; Jood, P.; Takabatake, T. Addition of Co, Ni, Fe and Their Role in the Thermoelectric Properties of Colusite $Cu_{26}Nb_2Ge_6S_{32}$. *J. Alloys Compd.* **2018**, *735*, 1838–1845.

(15) Suekuni, K.; Shimizu, Y.; Nishibori, E.; Kasai, H.; Saito, H.; Yoshimoto, D.; Hashikuni, K.; Bouyrie, Y.; Chetty, R.; Ohta, M.; Guilmeau, E.; Takabatake, T.; Watanabe, K.; Ohtaki, M. Atomic-Scale Phonon Scatterers in Thermoelectric Colusites with a Tetrahedral Framework Structure. *J. Mater. Chem. A* **2019**, *7* (1), 228–235. https://doi.org/10.1039/c8ta08248k.

(16) Bouyrie, Y.; Ohta, M.; Suekuni, K.; Kikuchi, Y.; Jood, P.; Yamamoto, A.; Takabatake, T. Enhancement in the Thermoelectric Performance of Colusites $Cu_{26}A_2E_6S_{32}$ (A = Nb, Ta; E = Sn, Ge) Using E-Site Non-Stoichiometry. *J. Mater. Chem. C* **2017**, *5* (17), 4174–4184. https://doi.org/10.1039/c7tc00762k.

(17) Bourgès, C.; Bouyrie, Y.; Supka, A. R.; Al Rahal Al Orabi, R.; Lemoine, P.; Lebedev, O. I.; Ohta, M.; Suekuni, K.; Nassif, V.; Hardy, V.; Daou, R.; Miyazaki, Y.; Fornari, M.; Guilmeau, E. High-Performance Thermoelectric Bulk Colusite by Process Controlled Structural Disordering. *J. Am. Chem. Soc.* **2018**, *140* (6), 2186–2195. https://doi.org/10.1021/jacs.7b11224.

(18) Kikuchi, Y.; Bouyrie, Y.; Ohta, M.; Suekuni, K.; Aihara, M.; Takabatake, T. Vanadium-Free Colusites $Cu_{26}A_2Sn_6S_{32}$ (A = Nb, Ta) for Environmentally Friendly Thermoelectrics. *J. Mater. Chem. A* **2016**, *4* (39), 15207–15214. https://doi.org/10.1039/C6TA05945G.

(19) Pavan Kumar, V.; Supka, A. R.; Lemoine, P.; Lebedev, O. I.; Raveau, B.; Suekuni, K.; Nassif, V.; Al Rahal Al Orabi, R.; Fornari, M.; Guilmeau, E. High Power Factors of Thermoelectric Colusites $Cu_{26}T_2Ge_6S_{32}$ (T = Cr, Mo, W): Toward Functionalization of the Conductive "Cu–S" Network. *Adv. Energy Mater.* **2019**, *9* (6), 1803249. https://doi.org/10.1002/aenm.201803249.

(20) Hagiwara, T.; Suekuni, K.; Lemoine, P.; Supka, A. R.; Chetty, R.; Guilmeau, E.; Raveau, B.; Fornari, M.; Ohta, M.; Al Rahal Al Orabi, R.; Saito, H.; Hashikuni, K.; Ohtaki, M. Key Role of d^0 and d^{10} Cations for the Design of Semiconducting Colusites: Large Thermoelectric *ZT* in $Cu_{26}Ti_2Sb_6S_{32}$ Compounds. *Chem. Mater.* **2021**, *33* (9), 3449–3456. https://doi.org/10.1021/acs.chemmater.1c00872.

(21) Zhang, R.-Z.; Chen, K.; Du, B.; Reece, M. J. Screening for Cu–S Based Thermoelectric Materials Using Crystal Structure Features. *J. Mater. Chem. A* **2017**, *5*, 5013. https://doi.org/10.1039/c6ta10607b.

(22) Pavan Kumar, V.; Barbier, T.; Caignaert, V.; Raveau, B.; Daou, R.; Malaman, B.; Caër, G. Le; Lemoine, P.; Guilmeau, E. Copper Hyper-Stoichiometry: The Key for the Optimization of Thermoelectric Properties in Stannoidite $Cu_{8+x}Fe_{3-x}Sn_2S_{12}$. *J. Phys. Chem. C* **2017**, *121* (30), 16454–16461. https://doi.org/10.1021/acs.jpcc.7b02068.

(23) Xie, H.; Su, X.; Zhang, X.; Hao, S.; Bailey, T. P.; Stoumpos, C. C.; Douvalis, A. P.; Hu, X.; Wolverton, C.; Dravid, V. P.; Uher, C.; Tang, X.; Kanatzidis, M. G. Origin of Intrinsically Low Thermal Conductivity in Talnakhite $Cu_{17.6}Fe_{17.6}S_{32}$ Thermoelectric Material: Correlations between Lattice Dynamics and Thermal Transport. *J. Am. Chem. Soc.* **2019**, *141* (27), 10905–10914. https://doi.org/10.1021/jacs.9b05072.

(24) Pavan Kumar, V.; Paradis-Fortin, L.; Lemoine, P.; Le Caër, G.; Malaman, B.; Boullay, P.; Raveau, B.; Guélou, G.; Guilmeau, E. Crossover from Germanite to Renierite-Type Structures in $Cu_{22-x}Zn_xFe_8Ge_4S_{32}$ Thermoelectric Sulfides. *ACS Appl. Energy Mater.* **2019**, *2* (10), 7679–7689. https://doi.org/10.1021/acsaem.9b01681.

(25) Paradis-Fortin, L.; Guélou, G.; Pavan Kumar, V.; Lemoine, P.; Prestipino, C.; Merdrignac-Conanec, O.; Durand, G. R.; Cordier, S.; Lebedev, O. I.; Guilmeau, E. Structure, Microstructure and Thermoelectric Properties of Germanite-Type $Cu_{22}Fe_8Ge_4S_{32}$ Compounds. *J. Alloys Compd.* **2020**, *831*, 154767. https://doi.org/10.1016/j.jallcom.2020.154767.

(26) Pavan Kumar, V.; Paradis-Fortin, L.; Lemoine, P.; Caignaert, V.; Raveau, B.; Malaman, B.; Le Caër, G.; Cordier, S.; Guilmeau, E. Designing a Thermoelectric Copper-Rich Sulfide from a Natural Mineral: Synthetic Germanite $Cu_{22}Fe_8Ge_4S_{32}$. *Inorg. Chem.* **2017**, *56* (21), 13376–13381. https://doi.org/10.1021/acs.inorgchem.7b02128.

(27) Lemoine, P.; Guélou, G.; Raveau, B.; Guilmeau, E. Crystal Structure Classification of Copper-Based Sulfides as a Tool for the Design of Inorganic Functional Materials. *Angew. Chem. Int. Ed.* **2022**, *61* (2). https://doi.org/10.1002/anie.202108686.

(28) Slack, G. A. *Handbook of Thermoelectrics* - CRC Press Book.; 1995.

(29) Wang, H.; Pei, Y.; LaLonde, A. D.; Jeffrey Snyder, G. Material Design Considerations Based on Thermoelectric Quality Factor. In *Thermoelectric nanomaterials*; 2013; pp 3–32. https://doi.org/10.1007/978-3-642-37537-8_1.

(30) Cohn, J. L.; Chakoumakos, B. C. Glass-Like Heat Conduction in Crystalline Semiconductors. *Phys. Rev. Lett.* **1999**, *82* (4), 779–782.

(31) Vineis, C. J.; Shakouri, A.; Majumdar, A.; Kanatzidis, M. G. Nanostructured Thermoelectrics: Big Efficiency Gains from Small Features. *Adv. Mater.* **2010**, *22* (36), 3970–3980. https://doi.org/10.1002/adma.201000839.

(32) Beekman, M.; Morelli, D. T.; Nolas, G. S. Better Thermoelectrics through Glass-like Crystals. *Nat. Mater.* **2015**, *14* (12), 1182–1185. https://doi.org/10.1038/nmat4461.

(33) Roychowdhury, S.; Biswas, R. K.; Dutta, M.; Pati, S. K.; Biswas, K. Phonon Localization and Entropy-Driven Point Defects Lead to Ultralow Thermal Conductivity and Enhanced Thermoelectric Performance in (SnTe)1-2 x(SnSe)x(SnS)x. *ACS Energy Lett.* **2019**, *4* (7), 1658–1662. https://doi.org/10.1021/acsenergylett.9b01093.

(34) Nolas, G. S.; Morelli, D. T.; Tritt, T. M. SKUTTERUDITES: A Phonon-Glass-Electron Crystal Approach to Advanced Thermoelectric Energy Conversion Applications. *Annu. Rev. Mater. Sci.* **2002**. https://doi.org/10.1146/annurev.matsci.29.1.89.

(35) Shimizu, Y.; Suekuni, K.; Saito, H.; Lemoine, P.; Guilmeau, E.; Raveau, B.; Chetty, R.; Ohta, M.; Takabatake, T.; Ohtaki, M. Synergistic Effect of Chemical Substitution and Insertion on the Thermoelectric Performance of $Cu_{26}V_2Ge_6S_{32}$ Colusite. *Inorg. Chem.* **2021**, *60* (15), 11364–11373. https://doi.org/10.1021/acs.inorgchem.1c01321.

(36) Kumar, V. P.; Lemoine, P.; Carnevali, V.; Guélou, G.; Lebedev, O. I.; Raveau, B.; Al Rahal Al Orabi, R.; Fornari, M.; Candolfi, C.; Prestipino, C.; Menut, D.; Malaman, B.; Juraszek, J.; Suekuni, K.; Guilmeau, E. Local-Disorder-Induced Low Thermal Conductivity in Degenerate Semiconductor $Cu_{22}Sn_{10}S_{32}$. *Inorg. Chem.* **2021**, *60* (21), 16273–16285. https://doi.org/10.1021/acs.inorgchem.1c02105.

(37) Zhang, R.-Z.; Gucci, F.; Zhu, H.; Chen, K.; Reece, M. J. Data-Driven Design of Ecofriendly Thermoelectric High-Entropy Sulfides. *Inorg. Chem.* **2018**, *57* (20), 13027–13033. https://doi.org/10.1021/acs.inorgchem.8b02379.

(38) Kumar, V. P.; Guélou, G.; Lemoine, P.; Raveau, B.; Supka, A. R.; Orabi, R. A. R. A.; Fornari, M.; Suekuni, K.; Guilmeau, E. Copper-Rich Thermoelectric Sulfides: Size-Mismatch Effect and Chemical Disorder in the [TS4]Cu6 Complexes of Cu26T2Ge6S32 (T=Cr, Mo, W) Colusites. *Angew. Chem. Int. Ed.* **2019**, *58* (43), 15455–15463. https://doi.org/10.1002/anie.201908579.

(39) Jiang, Q.; Yan, H.; Lin, Y.; Shen, Y.; Yang, J.; Reece, M. J. Colossal Thermoelectric Enhancement in Cu2+xZn1−xSnS4 Solid Solution by Local Disordering of Crystal Lattice and Multi-Scale Defect Engineering. *J. Mater. Chem. A* **2020**, *8* (21), 10909–10916. https://doi.org/10.1039/D0TA01595D.

(40) Hirayama, S.; Suekuni, K.; Sauerschnig, P.; Ohta, M.; Ohtaki, M. Cu–S-Based Thermoelectric Compounds with a Sphalerite-Derived Disordered Crystal Structure. *J. Solid State Chem.* **2022**, *309*, 122960. https://doi.org/10.1016/j.jssc.2022.122960.

(41) Raveau, B. Copper Mixed Valence Concept: "Cu(I)–Cu(II)" in Thermoelectric Copper Sulfides—an Alternative to "Cu(II)–Cu(III)" in Superconducting Cuprates. *J. Supercond. Nov. Magn.* **2020**, *33* (1), 259–263. https://doi.org/10.1007/s10948-019-05354-8.

(42) Tettenhorst, R. T.; Corbato, C. E. Crystal Structure of Germanite, $Cu_{26}Ge_4Fe_4S_{32}$, Determined by Powder X-Ray Diffraction. *Am. Mineral.* **1984**, *69* (9–10), 943–947.

(43) Nakao, H.; Ohwada, K.; Takesue, N.; Fujii, Y.; Isobe, M.; Ueda, Y.; Zimmermann, M. V.; Hill, J. P.; Gibbs, D.; Woicik, J. C.; Koyama, I.; Murakami, Y. X-Ray Anomalous Scattering Study of a Charge-Ordered State in NaV_2O_5. *Phys. Rev. Lett.* **2000**, *85* (20), 4349–4352. https://doi.org/10.1103/PhysRevLett.85.4349.

(44) Oeckler, O.; Stadler, F.; Rosenthal, T.; Schnick, W. Real Structure of $SrSi_2O_2N_2$. *Solid State Sci.* **2007**, *9* (2), 205–212. https://doi.org/10.1016/j.solidstatesciences.2006.11.009.

(45) Oeckler, O.; Schneider, M. N.; Fahrnbauer, F.; Vaughan, G. Atom Distribution in $SnSb_2Te_4$ by Resonant X-Ray Diffraction. *Solid State Sci.* **2011**, *13* (5), 1157–1161. https://doi.org/10.1016/j.solidstatesciences.2010.12.043.

(46) Schmidt, R.; Ströbele, M.; Romao, C. P.; Enseling, D.; Jüstel, T.; Meyer, H. J. Synthesis, Structure and Properties of a Calcium Oxonitridosilicate Phosphor Showing Green or Red Luminescence upon Doping with Eu^{2+} or Ce^{3+}. *Dalton Trans.* **2019**, *48* (37), 14069–14076. https://doi.org/10.1039/c9dt02564b.

(47) Heinke, F.; Urban, P.; Werwein, A.; Fraunhofer, C.; Rosenthal, T.; Schwarzmüller, S.; Souchay, D.; Fahrnbauer, F.; Dyadkin, V.; Wagner, G.; Oeckler, O. Cornucopia of Structures in the Pseudobinary System $(SnSe)_xBi_2Se_3$: A Crystal-Chemical Copycat. *Inorg. Chem.* **2018**, *57* (8), 4427–4440. https://doi.org/10.1021/acs.inorgchem.8b00105.

(48) Attfield, J. P. Determination of Valence and Cation Distributions by Resonant Powder X-Ray Diffraction. *Nature* **1990**, *343* (6253), 46–49. https://doi.org/10.1038/343046a0.

(49) Prandl, W. Phase Determination and Patterson Maps from Multiwave Powder Data. *Acta Crystallogr. Sect. A* **1990**, *46* (12), 988–992. https://doi.org/10.1107/S0108767390008819.

(50) Cheetham, A. K.; Wilkinson, A. P. Structure Determination and Refinement with Synchrotron X-Ray Powder Diffraction Data. *J. Phys. Chem. Solids* **1991**, *52* (10), 1199–1208. https://doi.org/10.1016/0022-3697(91)90194-5.
(51) Cheetham, A. K.; Wilkinson, A. P. Synchrotron X-ray and Neutron Diffraction Studies in Solid-State Chemistry. *Angew. Chem. Int. Ed. Engl.* **1992**, *31* (12), 1557–1570. https://doi.org/10.1002/anie.199215571.
(52) Morris, R. E.; Harrison, W. T. A.; Nicol, J. M.; Wilkinson, A. P.; Cheetham, A. K. Determination of Complex Structures by Combined Neutron and Synchrotron X-Ray Powder Diffraction. *Nature* **1992**, *359*, 519–522.
(53) Többens, D. M.; Gunder, R.; Gurieva, G.; Marquardt, J.; Neldner, K.; Valle-Rios, L. E.; Zander, S.; Schorr, S. Quantitative Anomalous Powder Diffraction Analysis of Cation Disorder in Kesterite Semiconductors. *Powder Diffr.* **2016**, *31* (3), 168–175. https://doi.org/10.1017/S0885715616000191.
(54) Gurieva, G.; Többens, D. M.; Levcenco, S.; Unold, T.; Schorr, S. Cu/Zn Disorder in Stoichiometric $Cu_2ZnSn(S_{1-x}Se_x)_4$ Semiconductors: A Complimentary Neutron and Anomalous X-Ray Diffraction Study. *J. Alloys Compd.* **2020**, *846*, 156304. https://doi.org/10.1016/j.jallcom.2020.156304.
(55) Lafond, A.; Choubrac, L.; Guillot-Deudon, C.; Deniard, P.; Jobic, S. Crystal Structures of Photovoltaic Chalcogenides, an Intricate Puzzle to Solve: The Cases of CIGSe and CZTS Materials. *Z. Anorg. Allg. Chem.* **2012**, *638* (15), 2571–2577. https://doi.org/10.1002/zaac.201200279.
(56) Helliwell, J. R.; Helliwell, M.; Jones, R. H. Ab Initio Structure Determination Using Dispersive Differences from Multiple-Wavelength Synchrotron-Radiation Powder Diffraction Data. *Acta Crystallogr. A* **2005**, *61* (6), 568–574. https://doi.org/10.1107/S010876730503237X.
(57) Sibille, R.; Mazet, T.; Malaman, B.; Wang, Q.; Didelot, E.; François, M. Site-Dependent Substitutions in Mixed-Metal Metal-Organic Frameworks: A Case Study and Guidelines for Analogous Systems. *Chem. Mater.* **2015**, *27* (1), 133–140. https://doi.org/10.1021/cm503570f.
(58) Hendrickson, W. A.; Teeter, M. M. Structure of the Hydrophobic Protein Crambin Determined Directly from the Anomalous Scattering of Sulphur. *Nature* **1981**, *290* (5802), 107–113. https://doi.org/10.1038/290107a0.
(59) Hendrickson, W. A. Determination Macromolecular Structures from Anomalous Diffraction of Synchrotron Radiation. *Science* **1991**, *254* (5028), 51–58.
(60) Cianci, M.; Helliwell, J. R.; Helliwell, M.; Kaucic, V.; Logar, N. Z.; Mali, G.; Tusar, N. N. Anomalous Scattering in Structural Chemistry and Biology. *Crystallogr. Rev.* **2005**, *11* (4), 245–335. https://doi.org/10.1080/08893110500421268.
(61) Okube, M.; Oshiumi, T.; Nagase, T.; Miyawaki, R.; Yoshiasa, A.; Sasaki, S.; Sugiyama, K. Site Occupancy of Fe^{2+}, Fe^{3+} and Ti^{4+} in Titanomagnetite Determined by Valence-Difference Contrast in Synchrotron X-Ray Resonant Scattering. *J. Synchrotron Radiat.* **2018**, *25* (6), 1694–1702. https://doi.org/10.1107/S1600577518013954.
(62) Boschini, F.; Minola, M.; Sutarto, R.; Scierle, E.; Bluschke, M.; Das, S.; Yang, Y.; Michiardi, M.; Shao, Y. C.; Feng, X.; Ono, S.; Zhong, R. D.; Schneeloch, J. A.; Gu, G. D.; Weschke, E.; He, F.; Chuang, Y. D.; Keimer, B.; Damascelli, A.; Frano, A.; da Silva Neto, E. H. Dynamic Electron Correlations with Charge Order Wavelength

along All Directions in the Copper Oxide Plane. *Nat. Commun.* **2021**, *12* (1), 1–8. https://doi.org/10.1038/s41467-020-20824-7.

(63) Seibold, G.; Arpaia, R.; Peng, Y. Y.; Fumagalli, R.; Braicovich, L.; Castro, C. Di; Grilli, M.; Ghiringhelli, G. C.; Caprara, S. Strange Metal Behaviour from Charge Density Fluctuations in Cuprates. *Commun. Phys.* **2021**, *4* (1), 1–6. https://doi.org/10.1038/s42005-020-00505-z.

(64) Welzmiller, S.; Urban, P.; Fahrnbauer, F.; Erra, L.; Oeckler, O. Determination of the Distribution of Elements with Similar Electron Counts: A Practical Guide for Resonant X-Ray Scattering. *J. Appl. Crystallogr.* **2013**, *46* (3), 769–778. https://doi.org/10.1107/S0021889813008923.

(65) Burger, K.; Cox, D.; Papoular, R.; Prandl, W. The Application of Resonant Scattering Techniques to Ab Initio Structure Solution from Powder Data Using $SrSO_4$ as a Test Case. *J. Appl. Crystallogr.* **1998**, *31* (5), 789–797. https://doi.org/10.1107/S0021889898006293.

(66) Paradis-Fortin, L.; Lemoine, P.; Prestipino, C.; Kumar, V. P.; Raveau, B.; Nassif, V.; Cordier, S.; Guilmeau, E. Time-Resolved In Situ Neutron Diffraction Study of $Cu_{22}Fe_8Ge_4S_{32}$ Germanite: A Guide for the Synthesis of Complex Chalcogenides. *Chem. Mater.* **2020**, *32* (20), 8993–9000. https://doi.org/10.1021/acs.chemmater.0c03219.

(67) Bruker AXS Inc. M86-E01078 APEX2 User Manual. In *M86-E01078 APEX2 User Manual*; Bruker AXS Inc: Madison, 2006.

(68) Briois, V.; Fonda, E.; Belin, S.; Barthe, L.; La Fontaine, C.; Langlois, F.; Ribbens, M.; Villain, F. SAMBA: The 4–40 KeV X-Ray Absorption Spectroscopy Beamline at SOLEIL. In *UVX 2010 - 10e Colloque sur les Sources Cohérentes et Incohérentes UV, VUV et X ; Applications et Développements Récents*; Ile de Porquerolles, France, 2011; pp 41–47. https://doi.org/10.1051/uvx/2011006.

(69) Pettifer, R. F.; Borowski, M.; Loeffen, P. W. The Physics of Ionization Chambers – or How to Improve Your Signal-to-Noise Ratio for Transmission EXAFS Measurements. *J. Synchrotron Radiat.* **1999**, *6* (3), 217–219. https://doi.org/10.1107/S090904959900062X.

(70) Ravel, B.; Newville, M. ATHENA, ARTEMIS, HEPHAESTUS: Data Analysis for X-Ray Absorption Spectroscopy Using IFEFFIT. *J. Synchrotron Radiat.* **2005**, *12* (4), 537–541. https://doi.org/10.1107/S0909049505012719.

(71) Watts, B. Calculation of the Kramers-Kronig Transform of X-Ray Spectra by a Piecewise Laurent Polynomial Method. *Opt. Express* **2014**, *22* (19), 23628. https://doi.org/10.1364/OE.22.023628.

(72) Sasaki, Satoshi. *Numerical Tables of Anomalous Scattering Factors Calculated by the Cromer and Liberman's Method*; Japan, 1989; p 137.

(73) Evans, G.; Pettifer, R. F. CHOOCH: A Program for Deriving Anomalous-Scattering Factors from X-Ray Fluorescence Spectra. *J. Appl. Crystallogr.* **2001**, *34* (1), 82–86.

(74) Belissont, R.; Muñoz, M.; Boiron, M.-C.; Luais, B.; Mathon, O. Distribution and Oxidation State of Ge, Cu and Fe in Sphalerite by μ-XRF and K-Edge μ-XANES: Insights into Ge Incorporation, Partitioning and Isotopic Fractionation. *Geochim. Cosmochim. Acta* **2016**, *177*, 298–314. https://doi.org/10.1016/j.gca.2016.01.001.

(75) Kumar, V. P.; Lemoine, P.; Carnevali, V.; Guélou, G.; Lebedev, O. I.; Boullay, P.; Raveau, B.; Orabi, R. A. R. A.; Fornari, M.; Prestipino, C.; Menut, D.; Candolfi, C.; Malaman, B.; Juraszek, J.; Guilmeau, E. Ordered Sphalerite Derivative Cu5Sn2S7: A Degenerate Semiconductor with High Carrier Mobility in the Cu–Sn–S Diagram. *J. Mater. Chem. A* **2021**, *9* (17), 10812–10826. https://doi.org/10.1039/D1TA01615F.

(76) Belissont, R.; Munoz, M.; Boiron, M.-C.; Luais, B.; Mathon, O. Germanium Crystal Chemistry in Cu-Bearing Sulfides from Micro-XRF Mapping and Micro-XANES Spectroscopy. *Minerals* **2019**, *9* (4), 227. https://doi.org/10.3390/min9040227.

(77) Szymanski, J. T. The Crystal Structure of Mawsonite, Cu 6 Fe 2 SnS 8. *Can. Mineral.* **1976**, *14* (4), 529–535.

(78) Hall, S. R.; Gabe, E. J. The Crystal Structure of Talnakhite, Cu18Fe16S32.1. *Am. Mineral.* **1972**, *57* (3-4_Part_1), 368–380.

(79) Bernstein, L. R.; Reichel, D. G.; Merlino, S. Renierite Crystal Structure Refined From Rietveld Analysis Of Powder Neutron-Diffraction Data. *Am. Mineral.* **1989**, *74* (9–10), 1177–1181.

(80) Hall, S. R.; Rowland, J. F. The Crystal Structure of Synthetic Mooihoekite Cu9Fe9S16. *Acta Crystallogr. B* **1973**, *29* (11), 2365–2372.

(81) Rowland, J. F.; Hall, S. R. Haycockite, $Cu_4Fe_5S_8$: A Superstructure in the Chalcopyrite Series. *Acta Crystallogr. B* **1975**, *31* (8), 2105–2112.

(82) Rodríguez-Carvajal, J. Recent Advances in Magnetic Structure Determination by Neutron Powder Diffraction. *Phys. B Condens. Matter* **1993**, *192* (1–2), 55–69. https://doi.org/10.1016/0921-4526(93)90108-I.

(83) Nenasheva, S. N. On the chemical composition of germanite. *Mineral. Mus. Collect.* **2003**, 34.

(84) Spiridonov, E. M. Maikainite $Cu_{20}(Fe,Cu_6Mo_2Ge_6S_{32}$ and Ovamboite $Cu_{20}(Fe,Cu,Zn)_6W_2Ge_6S_{32}$: New Minerals in Massive Sulfide Base Metal Ores. *Doklady Earth Sciences* **2003**, *393A* (9), 1329–1332.

(85) Suekuni, K.; Kim, F. S.; Nishiate, H.; Ohta, M.; Tanaka, H. I.; Takabatake, T. High-Performance Thermoelectric Minerals: Colusites Cu26V2M6S32 (M = Ge, Sn). *Appl. Phys. Lett.* **2014**, *105* (13), 132107. https://doi.org/10.1063/1.4896998.

(86) Lemoine, P.; Pavan Kumar, V.; Guélou, G.; Nassif, V.; Raveau, B.; Guilmeau, E. Thermal Stability of the Crystal Structure and Electronic Properties of the High Power Factor Thermoelectric Colusite Cu26Cr2Ge6S32. *Chem. Mater.* **2020**, *32* (2), 830–840. https://doi.org/10.1021/acs.chemmater.9b04378.

TOC

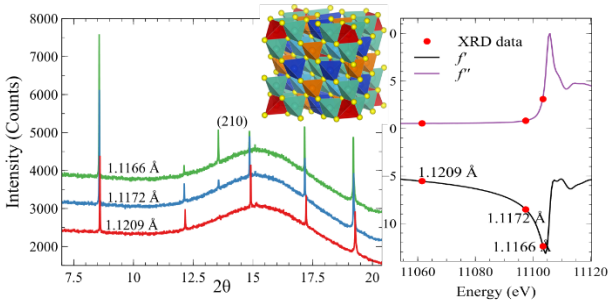
Intensity (Counts)
2θ
(210)
1.1166 Å
1.1172 Å
1.1209 Å
XRD data
f'
f''
Energy (eV)